Synthetic Aperature LADAR: A Model-Based Approach

Casey J. Pellizzari, Russell Trahan III, Hanying Zhou, Skip Williams, Stacie E. Williams, Bijan Nemati, Michael Shao, and Charles A. Bouman, *Fellow, IEEE,*

Abstract—Synthetic aperture LADAR (SAL) allows high resolution imaging of distant objects. Basic SAL image processing is based on Fast Fourier Transform (FFT) techniques originally developed for use in radar. These techniques can amplify noise and limit resolution. More advanced reconstruction techniques have been proposed for synthetic aperture radar (SAR), but have not been adapted for SAL. In addition, both conventional SAL and advanced SAR algorithms reconstruct the complex-valued reflection coefficient instead of the real-valued reflectance which leads to speckled images.

In this paper, we present a model-based iterative reconstruction (MBIR) algorithm designed specifically for SAL. Rather than estimating the reflection coefficient, we propose estimating its variance which is equal to the reflectance, a function that more closely resembles conventional optical images. A Bayesian framework is used to find the maximum a posteriori (MAP) estimate for the reflectance using a Q-Generalized Gaussian Markov Random Field (QGGMRF) prior model. The QGGMRF is able to model complex correlations between neighboring pixels which promotes a smooth and more natural looking image. The expectation-maximization (EM) algorithm is used to derive a surrogate for the MAP cost function. Finally, the proposed MBIR algorithm is tested on both simulated and experimental data. Results show significant and consistent improvements over existing reconstruction techniques in terms of image contrast, speckle reduction, autofocus, and low signal-to-noise ratio performance.

Index Terms—Synthetic Aperture LADAR, model-based iterative reconstruction, maximum a posteriori estimate, speckle reduction

I. INTRODUCTION

SPOTLIGHT-MODE synthetic aperture laser radar (SAL) allows high-resolution imaging beyond the diffraction limit of conventional optics. It is based on the same concept as synthetic aperture radar (SAR); however, SAL uses coherent laser radar (LADAR) at optical wavelengths, instead of the microwaves used in SAR.

While the concept of SAL is similar to SAR, the much shorter wavelength of light versus microwaves has a number of profound implications. First, the short wavelengths used for SAL allow high resolution images to be obtained with much smaller synthetic apertures than is possible with SAR. Second, at optical wavelengths, the micro structures of objects act as scatterers. Therefore, each SAL pixel typically contains

C. J. Pellizzari and C. A. Bouman are with the School of Electrical and Computer Engineering, Purdue University, West Lafayette, IN, 47907 USA e-mail: cpellizz@purdue.edu

S. Williams and S. E. Williams are with Air Force Research Laboratory, Maui HI.

R. Trahan, H. Zhou, B. Nemati, and M. Shao are with the Jet Propulsion Laboratory, California Institute of Technology, Pasadena, CA.

many scatterers resulting in images that more closely resemble conventional optical images. This contrasts with SAR images that are typically formed from groupings of large discrete scatters known as point clouds.

Despite the differences, modern SAL image processing is based on the Fourier reconstruction techniques initially used in SAR [1]–[6], specifically stretch or deramp processing [7], [8]. These techniques assume that the collected data can be approximated as spatial-frequency information on a Cartesian grid; hence a windowed, fast Fourier transform (FFT) is used to estimate the complex-valued reflection coefficient of the object [8]. Images are commonly formed by taking the amplitude squared of the reflection coefficient.

FFT-based reconstructions (FBR) have several undesirable characteristics. First, they tend to amplify noise and overfit the data. They also suffer from low resolution and artifacts due to sidelobes. Finally, and perhaps most importantly, they produce an estimate of the magnitude squared of the reflection coefficient, creating a speckled image with high variation that can obscure image details.

More specifically, if we denote the reflection coefficient by the complex number g, then g will have uniformly distributed phase for a surface that is rough relative to the wavelength [9]. This uniformly distributed phase implies that $|g|$ will have rapid spatial variation, and this rapid variation is conventionally known as speckle. However, the reflectance defined by

$$r = E[|g|^2], \quad (1)$$

is much smoother spatially because it is given by the expectation of the reflection coefficient [10], [11]. For the application of SAL, the reflectance, r, is of greater interest since it is proportional to the expected energy reflected from the object.

More advanced techniques have been developed for SAR image processing but have not been adapted for non-sparse scenes encountered in SAL. These advanced techniques have moved away from Fourier reconstructions towards regularized inversion methods [12]–[22]. Such approaches have largely been based on a Bayesian framework, either explicitly or implicitly, and can be viewed as finding the maximum a posteriori (MAP) estimate of the reflection coefficient using sparsity-inducing priors [13].

The advanced SAR techniques which assume sparsity in the image domain can be characterized into two main groups based on the type of prior model used. The first group of sparsity-enforcing approaches is known as sparse reconstruction or compressed sensing [12]–[18]. These techniques

generally use an L1 norm on the magnitude of the reflection coefficient, which can be considered a Laplacian prior in the Bayesian framework. Ren and Sun have proposed the adaptation of sparse reconstruction methods to the SAL problem [23]. Their method was shown to be robust to missing aperture data. However, the L1 norm regularization implicitly assumes sparse point clouds of scatterers, which is typically not the case for SAL imaging scenarios. This limits the effectiveness of regularization and results in speckled reconstructions.

The second group of sparsity-enforcing approaches which share some similarities with this work are based on Sparse Bayesian Learning (SBL) and Variational Bayesian Approximation (VBA) [19]–[22], [24], [25]. They assume the prior distribution of the reflection coefficient, g, is a zero-mean complex Gaussian which is independent but not identically distributed. At each point, the reflectance (i.e., the variance of the reflection coefficient) is modeled as an independent Gamma distributed hyper parameter [25]. SBL and VBA have been shown to outperform sparse reconstruction techniques at low signal-to-noise ratios (SNR) [20]. However, once again these algorithms are designed to reconstruct the spatial point clouds that occur in SAR images. So they do not enforce spatial smoothness and they result in speckled reconstructions.

Cetin and Karl proposed an algorithm that promotes both sparsity and smoothness in the reconstruction by enforcing penalties on the L1 norms of the magnitude of the reflection coefficient and the gradient of the magnitude [12]. The algorithm, which we will refer to as Feature-Enhanced SAR (FESAR), uses the two penalty terms to suppress the noise while preserving image features. However, the algorithm was designed for SAR and is based on regularization of the reflection coefficient magnitude, $|g|$, rather than its expected value, r.

In this paper, we propose a model-based iterative reconstruction (MBIR) technique designed specifically for SAL which both leverages the benefits of Bayesian estimation and is grounded in the physics of optical radar. A preliminary version of our research was first published at [26]. The major contributions are:

1) Estimation of reflectance: Rather than estimating the reflection coefficient as is done in existing SAR and SAL imaging, we propose to estimate its variance which is equal to the reflectance [11]. The reflectance produces images which appear more like natural optical images and allows exploitation of high spatial correlation during regularization.

2) Bayesian Framework using an Appropriate Prior Model: A Bayesian approach is taken to find the MAP estimate of the reflectance and to compute unknown phase errors. The Q-Generalized Gaussian Markov Random Field (QGGMRF) is proposed as an appropriate physics-based choice for a prior distribution [27] of the reflectance. It can model intricate two-dimensional dependencies and promotes smoothness in the reconstructed image.

3) Tractable Cost Minimization using EM Algorithm: Finding the MAP estimate of the reflectance requires optimization of a nonconvex cost function, which can be difficult and computationally expensive. Therefore we use the EM algorithm

to derive a more-tractable surrogate function. The MAP/EM framework is also used to estimate nuisance parameters. These include phase errors that blur the reconstruction.

4) Verification using Simulated and Experimental Data: The proposed algorithm is tested using simulated data generated by the Air Force Research Laboratory's (AFRL's) simulation tool *SimISAL* [28]. Experiments are carried out to investigate how well the algorithm performs in low signal-to-noise ratio (SNR) conditions with i.i.d. uniformly distributed phase errors. Finally, the algorithm is tested on data produced in the bench-top SAL laboratory at NASA's Jet Propulsion Laboratory (JPL). Results show significant and consistent improvements over standard SAL FFT-based reconstructions in terms of image contrast, speckle reduction, autofocus, and low-noise performance.

II. ESTIMATION SCHEME

A. Variable of Interest

Prior to developing an estimation framework, we must first determine what we wish to recover. Fig. 1 presents an example imaging scenario for an Inverse SAL (ISAL) system, along with the various quantities of interest. In the scenario, a telescope transmits and receives pulses that travel through the atmosphere, and are reflected off of an object with a real-valued reflectance function r. The figure includes the phenomenon which can degrade images. These include a time-varying phase error $\phi(t)$ caused by the atmosphere, speckle variations in the magnitude of the reflection coefficient, g, and measurement noise σ_w^2. Most importantly Fig. 1 illustrates that there is a difference between the object's reflectance, r, which we are accustomed to seeing in conventional images, and the reflection coefficient, g, a byproduct of coherent imaging.

Let us denote $r \in \mathbb{R}^N$ and $g \in \mathbb{C}^N$ as a column vectors whose components represent the reflectance, and reflection coefficients, respectively, of individual pixels. For a natural image under ambient illumination, the reflectance at each pixel, r_i, is the incoherent sum of the reflectivity from many small scatters which make up a pixel. Alternatively, due to the coherent illumination, SAL measures the coherent sum of the scatterers reflectivity g_i. For surfaces which are rough relative to the observation wavelength, the value g_i at each pixel can be modeled as the sum of many complex numbers corresponding to individual scatters with random phase. Therefore, by the central limit theorem, we can accurately model g_i as a complex Gaussian random variable with zero mean and a variance equal to the reflectance r_i, in accordance with Eq. (1). The elements of g are spatially uncorrelated due to the i.i.d. uniformly distributed random phase. In addition, the spatial correlation of its magnitude is small. Therefore, direct regularization of g, $|g|$, or $|g|^2$ can not fully exploit the spatial correlation of the underlying reflectance, r.

To illustrate this, consider the one-dimensional example shown in Fig. 2. A reflectance vector r is given along with the corresponding reflection coefficient, g. It is easy to see that r is highly correlated between neighboring samples but $|g|$ is only loosely correlated, and the phase is completely uncorrelated and independent. Estimating the reflectance, r, instead of the
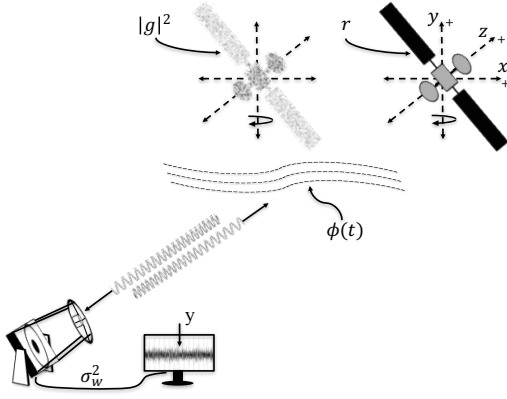
Fig. 1. Example concept for a ground based ISAL system used for imaging objects in space. The target has a reflection coefficient, g, with a variance at each point equal to the reflectance function r. The coordinate system x, y, z is centered on the object with z representing the line-of-sight vector. Object motion is a rotation around thy y-axis. The atmosphere imparts an unknown, time varying phase error $\phi(t)$. Finally, the noisy data y (with noise power σ_w^2) is recorded to disk for processing.
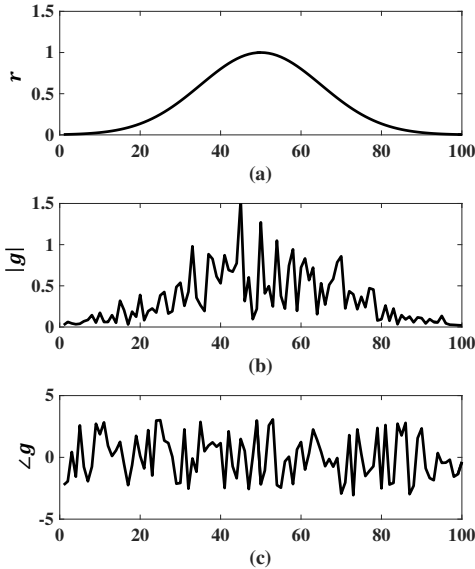

Fig. 2. Subplot (a) shows an example of a reflectance function r. Subplot (b) is the amplitude of the complex Gaussian reflectivity g corresponding to r. Subplot (c) shows the phase of g. Neighboring samples of r are highly correlated, however the amplitude of g is only loosely correlated and its phase is uncorrelated and independent.

reflection coefficient, g, enables us to fully utilize its spatial correlation when using a Bayesian framework. This helps to better constrain the estimation process and produces more natural looking images.

B. Bayesian Framework

Our goal is to compute the MAP estimate of r.[1] To do so, we must also estimate the phase errors, ϕ, and the noise

[1]In practice, the quantity we estimate is proportional to the actual reflectance by an unknown multiplicative constant α.

variance, σ_w^2. The joint estimates are given by

$$
\begin{aligned}
(\hat{r}, \hat{\phi}, \hat{\sigma}_w^2) &= \underset{r,\phi,\sigma_w^2 \in \Omega}{\arg\min} \left\{ -\log p_\theta(r|y) \right\}, \\
&= \underset{r,\phi,\sigma_w^2 \in \Omega}{\arg\min} \left\{ -\log p_\theta(y|r) - \log p(r) \right\},
\end{aligned} \tag{2}
$$

where Ω represents the jointly-feasible set and the subscript $\theta = [\phi, \sigma_w^2]$ indicates a dependance on the phase errors and noise variance.

To compute the likelihood function $p_\theta(y|r)$, we use the reflection coefficient vector, g, to relate the reflectance vector, r to the data vector, y. It will be shown that the conditional distribution of the data, given g and an additive white-noise model, is a complex Gaussian. Its distribution is given by

$$
p_\theta(y|g) = \frac{1}{\pi^M \left(\sigma_w^2\right)^M} \exp\left\{ -\frac{1}{\sigma_w^2} ||y - A_\phi g||_2^2 \right\}, \tag{3}
$$

where $y \in \mathbb{C}^M$, σ_w^2 is the noise variance, and $A \in \mathbb{C}^{M \times N}$ is the linear forward-model operator. The subscript ϕ indicates the dependance of A on the phase errors.

The components of the reflection coefficient vector, g, are uncorrelated but not independent since the components of r are not independent. However, g is conditionally independent given r. Therefore, we can write the joint, conditional probability distribution of the reflection coefficients given the reflectance as

$$
p(g|r) = \frac{1}{\pi^N |\mathcal{D}(r)|} \exp\left\{ -g^H \mathcal{D}(r)^{-1} g \right\}, \tag{4}
$$

where ^{H} indicates the Hermitian transpose and $\mathcal{D}(r)$ is a matrix with diagonal elements equal to the vector r. The resulting likelihood function is given by [29]

$$
p_\theta(y|r) = \frac{1}{\pi^N |C_{y|r,\theta}|} \exp\left\{ -y^H C_{y|r,\theta}^{-1} y \right\}, \tag{5}
$$

where

$$
C_{y|r,\theta} = A_\phi \mathcal{D}(r) A_\phi^H + \sigma_w^2 I . \tag{6}
$$

With the likelihood function specified in Eq. (5), the MAP cost function can be written as

$$
\begin{aligned}
f(r,\theta) &= -\log p_\theta(y|r) - \log p(r), \\
&= \log |C_{y|r,\theta}| + y^H C_{y|r,\theta}^{-1} y - \log p(r) .
\end{aligned} \tag{7}
$$

C. MAP Estimation Using the EM Algorithm

Optimization of Eq. (7) is not tractable due to the determinant and inverse in the likelihood function. Instead, we propose to use the EM algorithm to replace the cost function with a more tractable function. A logical choice for the missing data is the reflection coefficient, g. Given this choice, the replacement function is given by

$$
Q(r,\theta; r',\theta') = -\mathrm{E}\left[\log p_\theta(y, g | r) | Y = y, r', \theta'\right] - \log p(r), \tag{8}
$$

where r' and θ' are the current estimates of r and θ, respectively. In this paper we will only consider cases where A is a non-normalized unitary matrix. We will see that this allows us to compute Q exactly which constitutes the E-step of the EM algorithm. Fig. 3 shows the alternating minimization approach used for implementing the M-step of the EM algorithm.

Repeat{

$$\hat{r} \leftarrow \underset{r}{\operatorname{argmin}} \ Q(r, \theta'; r', \theta')$$

$$\hat{\theta} \leftarrow \underset{\theta}{\operatorname{argmin}} \ Q(r', \theta; r', \theta')$$

$$r' \leftarrow \hat{r}$$

$$\theta' \leftarrow \hat{\theta}$$

}

Fig. 3. Steps of the EM algorithm for joint optimization of the MAP cost function surrogate

The algorithm proposed in Fig. 3 inherits the standard convergence properties of the EM algorithm for problems of this nature. It can be shown that $Q(r, \theta; r', \theta')$ is an upper-bounding surrogate function such that minimization of Q implies minimization of f [30]–[33]. That is

$$\{Q(r, \theta; r', \theta') < Q(r', \theta'; r', \theta')\} \Rightarrow \{f(r, \theta) < f(r', \theta')\} \ . \tag{9}$$

Convergence properties of the EM algorithm are presented in [30]–[33]. In particular, Theorem 4.1 of [32], states that since f is monotonically decreased by the sequence of points generated from surrogate optimization, f converges to some limit f^*. Generally speaking, the EM algorithm converges in a stable manner to a local minima.

Since the MAP cost function is nonconvex, f^* will depend on the initial conditions and may not be the global minimum. Later, in Sec. IV.C, a heuristic is described which was found to be effective for initialization. In addition, like other noncon-vex problems, reconstruction may be ill-posed as defined by Tikhonov [34]. Specifically, stability is not guaranteed since the MAP estimate may not be a continuous function of the data.

The remaining sections of this paper are organized as follows: In Sec. III we provide a derivation of the forward model and present the QGGMRF as our prior. Section IV discusses the the EM algorithm. Specifically, we show how Q is computed using the posterior distribution of the hidden data, and we explain the optimization algorithm. Section V presents results of the proposed algorithm for both simulated and experimental data. Final conclusions are discussed in Sec. VI.

III. MEASUREMENT AND PRIOR MODELS

A. Continuous Measurement Model

Let $\tilde{g}(x, y, z)$ represent the continuous reflection-coefficient function for the object being imaged. Continuous functions for which we also introduce a discrete version will be denoted with a tilde. Using the object-centered coordinate system depicted in Fig. 1, it is assumed without loss of generality, that the object is rotating around the y axis. Given this geometry, a synthetic-aperture system is able to resolve a projection of the object in the $x - z$ plane given by

$$\tilde{g}(x, z) = \int_{-\infty}^{\infty} \tilde{g}(x, y, z) dy, \tag{10}$$

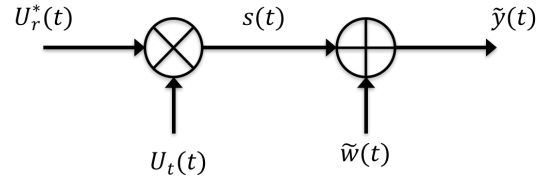subject to any shadowing for opaque objects.

Fig. 4. Simplified representation of the heterodyne detection process.

The linear-frequency-modulated (LFM) chirped waveform transmitted from a SAL system is given by the analytical function

$$U_t(t) = e^{j\phi_t(t)}, \quad \text{for } 0 \leq t \leq \tau_c, \tag{11}$$

with phase

$$\phi_t(t) = \omega_c t + \beta t^2, \tag{12}$$

where ω_c is the optical carrier frequency in radians, β is the chirp rate (2β has units of rad/s^2) and τ_c is the chirp length in seconds [8]. The spatial envelope of the transmitted pulse is assumed to be uniform across the $x - y$ plane and rectangular along the z dimension. In addition, the spatial length of the pulse is assumed to be much larger than the depth of the object being imaged.

The return field at the receiver is then given by

$$U_r(t) = \iint_{-\infty}^{\infty} \tilde{g}(x, z) e^{j\phi_r(t, x, z)} dx dz, \tag{13}$$

where the return phase from each point, $\phi_r(t, x, z)$, is a delayed version of the transmitted phase, plus any phase errors, given by

$$\phi_r(t, x, z) = \phi_t \left(t - \frac{2z}{c} - \frac{2\tilde{\varphi}(t)x}{c} \right) + \tilde{\phi}(t) \ . \tag{14}$$

The variable $\tilde{\varphi}(t)$ is the rotation angle of the object at time t, and $\tilde{\phi}(t)$ represents the time-varying phase errors. Without loss of generality, the overall propagation time between the transmitter and the object can be ignored.

Standard optical heterodyne detection is performed by mix-ing the received signal, $U_r(t)$, with a local oscillator formed by the transmitted signal, $U_t(t)$ [10], [11], [35]. The system is assumed to be shot-noise limited with noise driven by the power of the local oscillator. Fig. 4 presents a simplified representation of the detection process. The demodulated and filtered output signal is given by

$$\tilde{y}(t) = s(t) + \tilde{w}(t), \tag{15}$$

where $\tilde{w}(t)$ is additive, zero-mean, complex Gaussian white noise, and

$$\begin{aligned} s(t) &= U_t(t) U_r^*(t), \\ &= e^{-j\phi(t)} \iint_{-\infty}^{\infty} \tilde{g}(x, z) \ e^{j\Delta\phi(t, x, z)} dx dz, \end{aligned} \tag{16}$$

where $*$ indicates the complex conjugate. The phase $\Delta\phi(t,x,z)$, is the difference between the reference waveform phase and the return phase, and is given by

$$\Delta\phi(t,x,z) = \phi_t(t,x,z) - \phi_r(t,x,z)$$
$$= \frac{2\omega_c\tilde{\varphi}(t)x}{c} + \frac{4z\beta t}{c} + \frac{4\beta t\tilde{\varphi}(t)x}{c} + \frac{4\beta\tilde{\varphi}^2(t)x^2}{c^2}$$
$$+ \frac{8\beta z\tilde{\varphi}(t)x}{c^2} - \tilde{\phi}(t) + \phi_c, \tag{17}$$

where ϕ_c is the sum of all constant phase terms. The constant terms can be ignored since only the time-varying phase contributes to image formation. Terms in Eq. (17) with c^2 in the denominator are small and can be dropped. As shown in App. A, the term $4\beta t\tilde{\varphi}(t)x/c$ is also negligible for typical imaging scenarios. Therefore, Eq. (17) reduces to

$$\Delta\phi(t,x,z) \approx \frac{2\omega_c\tilde{\varphi}(t)x}{c} + \frac{4z\beta t}{c} - \tilde{\phi}(t),$$
$$\approx 2\pi\left[\frac{2\tilde{\varphi}(t)}{\lambda}x + \frac{2\beta t}{\pi c}z\right] - \tilde{\phi}(t) . \tag{18}$$

where $\lambda = 2\pi c/\omega_c$ is the laser wavelength. The resulting demodulated signal may therefore be approximated as

$$\tilde{y}(t) \approx e^{-j\tilde{\phi}(t)}\iint_{-\infty}^{\infty} \tilde{g}(x,z)\ e^{j2\pi\left[\frac{2\tilde{\varphi}(t)}{\lambda}x + \frac{2\beta t}{\pi c}z\right]}dxdz + \tilde{w}(t) . \tag{19}$$

B. Discrete Measurement Model

Equation (19) is continuous in time and space, and only valid for a single pulse duration. We wish to represent the signal as temporally discrete in terms of both the sample and pulse indices. For a system that transmits pulses back to back with period τ_c (i.e. 100% duty cycle), the qth sample of the pth pulse occurs at time

$$t = p\tau_c + q\tau_d, \tag{20}$$

where τ_d is the detector integration period. The temporally-discrete analytical signal can then be represented as

$$y(p,q) = \tilde{y}(p\tau_c + q\tau_d) . \tag{21}$$

We can also represent the continuous object, $\tilde{g}(x,z)$, as a discrete space signal, $g(k,l)$, using the relationship

$$\tilde{g}(x,z) = \sum_{k,l} g(k,l)\ \tilde{h}(x - k\delta_x, z - l\delta_z), \tag{22}$$

where $\tilde{h}$ is the interpolating basis function, δ_x, δ_z are the spatial sampling periods, and k,l are the sample indices. For a Nyquist-sampled, band-limited signal, $\tilde{h}$ is a $sinc$ with cutoff frequency $f_c = (1/\delta_x, 1/\delta_z)$. Substituting Eq. (22) into Eq. (21) results in

$$y(p,q) = e^{-j\phi(p,q)}\iint_{-\infty}^{\infty}\sum_{k,l} g(k,l)\ \tilde{h}(x - k\delta_x, z - l\delta_z)$$
$$* e^{j2\pi\left[\frac{2\varphi(p,q)}{\lambda}x + \frac{2\beta(p\tau_c + q\tau_d)}{\pi c}z\right]}dxdz + w(p,q), \tag{23}$$

where we define

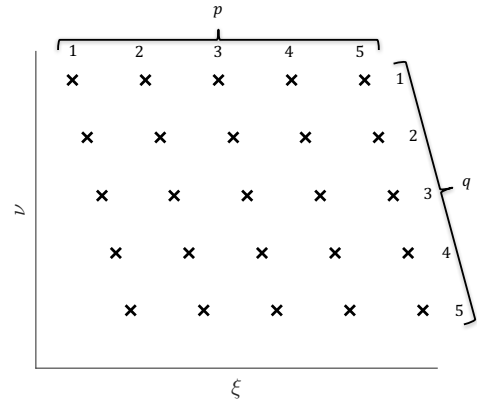$$\varphi(p,q) = \tilde{\varphi}(p\tau_c + q\tau_d), \tag{24}$$

Fig. 5. Skewed DSFT samples corresponding to Eq. (29) for a linearly rotating object. The Samples for each pulse span both dimensions in the spatial-frequency domain.

as the discrete rotation angle, and

$$\phi(p,q) = \tilde{\phi}(p\tau_c + q\tau_d), \tag{25}$$

as the discrete phase error function. The term $w(p,q)$ is the measurement noise at each sample which is assumed to be i.i.d. complex Gaussian with variance σ_w^2.

Equation (23) can be written more simply as

$$y(p,q) = e^{-j\phi(p,q)}\tilde{H}\left(-\frac{2\varphi(p,q)}{\lambda}, -\frac{2\beta q\tau_d}{\pi c}\right)$$
$$* G\left(-\frac{4\pi\varphi(p,q)\delta_x}{\lambda}, -\frac{4\beta q\tau_d\delta_z}{c}\right) + w(p,q), \tag{26}$$

where $\tilde{H}$ is the Continuous Space Fourier Transform (CSFT) of $\tilde{h}$ given by

$$\tilde{H}(u,v) = \iint_{-\infty}^{\infty} \tilde{h}(x,z)e^{-j2\pi(ux+vz)}, \tag{27}$$

and G is the discrete-space Fourier transform (DSFT) of g given by

$$G(\xi,\nu) = \sum_{k,l} g(k,l)e^{-j(\xi k + \nu l)} . \tag{28}$$

Given the form of Eq. (26) we see that the data are samples of the DSFT of $g(k,l)$ at frequencies

$$\xi(p,q) = -\frac{4\pi\varphi(p,q)\delta_x}{\lambda}, \quad \nu(q) = -\frac{4\beta q\tau_d\delta_z}{c} . \tag{29}$$

Note that the rotation angle φ, and therefore ξ, is a function of both p and q, whereas ν is only a function of q. For a constant rotational velocity we get linear changes in both phase terms from sample to sample, meaning that the data traces a diagonal line in the spatial-frequency domain. Fig. 5 shows a sample pattern in the frequency domain for such a case. As the object rotates over the period of a single pulse, the value of both ν and ξ change, creating a skewed pattern. In the special case that the sample locations can be approximated as a Cartesian grid with $\xi(p,q) \approx \xi(p)$, then G would correspond to the FFT of g. This approximation is commonly assumed in traditional SAL processing [1]–[6].

Equation (26) can be represented in matrix-vector notation as

$$y = Ag + w, \qquad (30)$$

where $y \in \mathbb{C}^M$, $g \in \mathbb{C}^N$, and $A \in \mathbb{C}^{M \times N}$. The measurement noise vector has a complex normal distribution given by

$$w \sim CN\left(0, \sigma_w^2 I\right), \qquad (31)$$

where I is the identity matrix. The linear forward model operator can be expanded as

$$A = \mathcal{D}(\phi)HD, \qquad (32)$$

where $\mathcal{D}(\phi) \in \mathbb{C}^{M \times M}$ is a diagonalization of the phase error vector ϕ, $H \in \mathbb{C}^{M \times M}$ is the reconstruction filter for the interpolation basis function, and $D \in \mathbb{C}^{M \times N}$ directly evaluates the DSFT samples of g.

In order to make evaluation of the sampled DSFT computationally tractable, advanced interpolation techniques such as the Nonuniform FFT (NUFFT) are required [36]. Such techniques have been designed to minimize error. Reference [36] approximates D as

$$D \approx VFS, \qquad (33)$$

where V is an $M \times K$ sparse interpolation matrix, F is a $K \times N$ oversampled DFT matrix with samples on a Cartesian grid, and S is a $N \times N$ matrix of scaling factors used by the NUFFT algorithm to minimize errors. Both V and S are found by minimizing the worst-case approximation error for a specific geometry. The matrix A can therefore be approximated as

$$A \approx \mathcal{D}(\phi)HVFS . \qquad (34)$$

C. Prior Model

A Q-Generalized Gaussian Markov Random Field (QG-GMRF) was used as a prior model [27]. QGGMRF is based on a pair-wise Gibbs distribution given by [33]

$$p(r) = \frac{1}{z} \exp\left\{ -\sum_{\{i,j\} \in \mathcal{P}} b_{i,j} \rho(\Delta) \right\}, \qquad (35)$$

where z is the partition function, $b_{i,j}$ is the weight between neighboring pixel pairs r_i and r_j, $\Delta = r_i - r_j$, $\mathcal{P}$ is the set of all pair-wise cliques falling within the same neighborhood, and $\rho(\cdot)$ is the potential function [33]. The QGGMRF potential function is given by

$$\rho\left(\frac{\Delta}{\sigma_r}\right) = \frac{|\Delta|^p}{p\sigma_r^p} \left(\frac{|\frac{\Delta}{T\sigma_r}|^{q-p}}{1 + |\frac{\Delta}{T\sigma_r}|^{q-p}} \right), \qquad (36)$$

where T is a unitless threshold value which controls the transition of the potential function from having the exponent q (typically $q = 2$) to having the exponent p. The variable σ_r controls the variation in $\hat{r}$.

The parameters of the QGGMRF potential function affect the influence neighboring pixels have on one another. As the value of p increases, pixels which are far apart in value have more influence on each other. This can help reduce variation due to noise but may also blur edges. As p decreases, the influence of pixels far in value is significantly decreased. This

helps preserve edges. Typically, p is greater than one (around 1.1 or 1.2) to ensure a strictly-convex prior model, and we vary T to control the influence function. The value of T controls how close in value pixels must be to have a strong influence on each other. For small T and $p \approx 1$, the potential function resembles that of a total-variation prior. For large T and $q = 2$, the potential function acts as that of a Gaussian prior for all but the most-differently-valued pixels. Finally, σ_r is used to control the amount of regularization. A large σ_r will lead to reconstructions with higher variation and that more-closely match the data. Lower values of σ_r reduce variation in the reconstruction.

While there are many prior models that can be used, such as those in [37]–[39], the utility of QGGMRF has been successfully demonstrated in practice for applications such as medical imaging [27]. The QGGMRF model is capable of simultaneously preserving edges and smoothing homogeneous areas. In addition, its potential function is both convex and continuously differentiable, which is important for optimization. Finally, the shape of the potential function can be easily tuned for the application at hand.

IV. ALGORITHM

In the following sections, we describe the steps of our algorithm. First, we derive a closed-form expression for Q. Second we propose a method to minimize Q based on alternating minimization of r and the parameters of θ. Lastly, we describe the initialization process, stopping criteria, and complexity.

A. Derivation of MAP Surrogate Function

With the forward and prior models specified, we can evaluate the surrogate $Q(r, \theta; r', \theta')$. To do so, we start by expanding the argument of the expectation in Eq. (8) using Bayes' theorem. This gives

$$\begin{aligned} Q(r, \theta; r', \theta') = & -\mathrm{E}\left[\log p_\theta(y|g, r) + \log p(g|r) \,|Y = y, r', \theta'\right] \\ & -\log p(r), \\ = & M \log \sigma_w^2 + \mathrm{E}\left[\frac{1}{\sigma_w^2}||y - A_\phi g||^2 \,|Y = y, r', \theta'\right] \\ & + \log|\mathcal{D}(r)| + \sum_{i=1}^{N} \frac{1}{r_i} \mathrm{E}\left[|g_i|^2 \,|Y = y, r', \theta'\right] \\ & + \sum_{\{i,j\} \in \mathcal{P}} b_{i,j} \rho\left(\frac{\Delta}{\sigma_r}\right), \end{aligned} \qquad (37)$$

where $p_\theta(y|g, r) = p_\theta(y|g)$.

In order to evaluate the expectation in Eq. (37), the conditional posterior distribution of g must be specified. Using Bayes' theorem, it can be written as

$$\begin{aligned} p_\theta(g|y, r) &= \frac{p_\theta(y|g)p(g|r)}{p_\theta(y|r)}, \\ &= \frac{1}{z} \exp\left\{ -\frac{1}{\sigma_w^2}||y - A_\phi g||^2 - g^H \mathcal{D}(r)^{-1} g \right\}, \end{aligned} \qquad (38)$$

where z is the partition function which has absorbed any exponential terms that are constant with respect to g. By

expanding the exponent and completing the square, it can be shown that the conditional posterior is a complex Gaussian with mean

$$\mu = C\frac{1}{\sigma_w^2}A_\phi^H y, \tag{39}$$

and covariance

$$C = \left[\frac{1}{\sigma_w^2}A_\phi^H A_\phi + \mathcal{D}(r)^{-1}\right]^{-1}. \tag{40}$$

To find μ, we use Gradient Descent with Line Search (GDLS) to maximize the posterior distribution with respect to g. Since the distribution is quadratic, the optimal step size can be computed in closed form [33].

Evaluation of the posterior covariance C requires inversion of a large and dense matrix. In this paper we will only consider cases where the object rotation is linear and $M = N$ (conditions which are the basis for all Fourier-based reconstructions). It is shown in App. B that when these conditions hold, A is a non-normalized unitary matrix which means $A^H A = MI$. For such cases, C becomes

$$C = \left[\frac{M}{\sigma_w^2}I + \mathcal{D}(r)^{-1}\right]^{-1} = \mathcal{D}\left(\frac{\sigma_w^2}{M + \frac{\sigma_w^2}{r}}\right). \tag{41}$$

For non-unitary cases, C must be computed directly, which is a non-trivial task, or approximations must be used.

With the posterior distribution specified, the expectation in Eq. (37) can be evaluated. The resulting final form of the MAP surrogate is given by

$$\begin{aligned} Q(r,\theta;r',\theta') = &M\log\sigma_w^2 + \frac{1}{\sigma_w^2}y^H y - \frac{1}{\sigma_w^2}2\mathrm{Re}\left\{y^H A_\phi \mu\right\} \\ &+ \frac{M}{\sigma_w^2}\sum_{i=1}^{N}\left(C_{i,i} + |\mu_i|^2\right) + \log|\mathcal{D}(r)| \\ &+ \sum_{i=1}^{N}\frac{1}{r_i}\left(C_{i,i} + |\mu_i|^2\right) \\ &+ \sum_{\{i,j\}\in\mathcal{P}}b_{i,j}\rho\left(\frac{\Delta}{\sigma_r}\right) + c. \end{aligned} \tag{42}$$

where c represents the terms constant with respect to r and θ.

B. Optimization of MAP Surrogate Function

As shown in Fig. 3, we use alternating minimization to implement the M-step of the EM algorithm. In the sections below, we derive the updates for the optimization with respect to r, ϕ, and σ_w^2, and we propose stoping criteria.

1) Reflectance Update: The positivity constraint on r and non-convex cost function given by Eq. (42) make Iterative Coordinate Descent (ICD) an attractive choice for optimization [33]. The update for the sth pixel is given by

$$r_s^* = \operatorname*{argmin}_{r_s\in\mathbb{R}^+}\left\{\log r_s + \frac{C_{s,s} + |\mu_s|^2}{r_s} + \sum_{j\in\partial s}b_{s,j}\rho\left(\frac{r_s - r_j}{\sigma_r}\right)\right\} \tag{43}$$

Minimization is carried out with a 1D line-search over $\mathbb{R}^+$.

2) Noise Power Update: Taking the derivative of Eq. (42) with respect to σ_w^2 and rooting provides a closed form solution for the update of the noise variance which is given by

$$\hat{\sigma}_w^2 = \frac{1}{M}y^H y - \frac{2}{M}\mathrm{Re}\left\{y^H A_\phi \mu\right\} + \sum_{i=1}^{N}\left(C_{i,i} + |\mu_i|^2\right). \tag{44}$$

3) Phase Error Estimation: The phase error vector is updated by minimizing Eq. (42) with respect to ϕ. The update is given by

$$\begin{aligned} \phi^* &= \operatorname*{argmin}_{\phi\in\Omega}\left\{-\mathrm{Re}\left(y^H A_\phi \mu\right) + c\right\}, \\ &= \operatorname*{argmin}_{\phi\in\Omega}\left\{-\mathrm{Re}\left(y^H \mathcal{D}(\phi)HD\mu\right) + c\right\}, \end{aligned} \tag{45}$$

where c are the terms in Eq. (42) which are constant with respect to ϕ. To simplify optimization we can write the elements of the phase error vector as $\phi_i = e^{\psi_i}$ and optimize over the real-valued phase, ψ_i, for each element. In addition, it is common that neighboring samples share the same phase error. For example, all samples of a single pulse may have the same atmospheric phase error when the pulse is short compared to the atmospheric coherence time. In such cases, the variance of the estimator can be reduced by averaging individual estimates [8]. Therefore, the estimated phase error for each group, p, is given by

$$\phi_p = e^{\psi_p^*}, \tag{46}$$

where

$$\psi_p^* = \operatorname*{argmin}_{\psi\in\Omega}\left\{-\mathrm{Re}\left(y_p^H e^{i\psi}[HD\mu]_p\right)\right\}, \tag{47}$$

The subscript p indicates that just the elements of the vector belonging to the group p are used.

4) Stopping Criteria: To determine when the algorithm should be stopped, we can use either a set number of iterations, N_K, or a metric such as

$$\epsilon = \frac{||r^k - r^{k-1}||}{||r^{k-1}||}, \tag{48}$$

where k is the iteration index, and the algorithm is stopped when ϵ falls below a threshold value of ϵ_T. Fig. 6 summarizes the steps of the EM algorithm

C. Initialization

We found that an iterative initialization process consistently produced initial conditions which resulted in focused images, even at very-low SNRs. Fig. 7 details the steps of this iterative process. The initial estimate of the phase-error vector is given by

$$\hat{\phi}_{PGA} = \mathrm{PGA}(y), \tag{49}$$

where the operator $\mathrm{PGA}(y)$ indicates the application of the standard Phase Gradient Autofocus (PGA) algorithm to y [8].

Next, for some set number of outer-loop iterations, N_L, we allow the EM algorithm to run for N_K iterations. At the

Iterative EM $\{$

Inputs: $y,\ r',\phi',\ \sigma_r,\ \sigma_w^{2'},\ q,\ p,\ T,\ b,$ (either N_K or ϵ_T)

Outputs: $\hat{r}, \hat{\phi}$

while $k < N_K$ or $\epsilon > \epsilon_T$ **do**

   $\mu \leftarrow \underset{g}{\mathrm{argmin}}\ \{-\log p_\theta(g|Y = y, r', \theta')\}$

   $C \leftarrow \mathcal{D}\left(\frac{\sigma_w^2}{M + \frac{\sigma_w^2}{r'}}\right)$

   for all $s \in S$ **do**

      $r_s = \underset{r_s \in \mathbb{R}^+}{\mathrm{argmin}}\left\{\log r_s + \frac{C_{s,s} + |\mu_s|^2}{r_s} + \sum_j b_{s,j}\rho\left(\frac{r_s - r_j}{\sigma_r}\right)\right\}$

   end for

   $\sigma_w^2 \leftarrow \frac{1}{M}y^H y - \frac{2}{M}\mathrm{Re}\left\{y^H A_\phi \mu\right\} + \sum_{i=1}^N \left(C_{i,i} + |\mu_i|^2\right)$

   for all $p \in P$ **do**

      $\psi_p^* = \underset{\psi \in \Omega}{\mathrm{argmin}}\left\{-\mathrm{Re}\left(y_p^H e^{i\psi}[HD\mu]_p\right)\right\}$

      $\phi_p \leftarrow e^{\psi_p^*}$

   end for

end while

$\}$

Fig. 6. EM algorithm for MAP estimate of r. S is the set of all pixels, P is the set of all pixel groups which share the same phase errors.

beginning of each outer-loop iteration, we initialize/reinitialize according to

$$r \leftarrow |A^H y|^{\circ 2},$$
$$\sigma_r \leftarrow \frac{1}{\gamma}\sqrt{\mathrm{var}(r)}, \tag{50}$$
$$\sigma_w^2 \leftarrow \mathrm{var}(y),$$

where $|\cdot|^{\circ 2}$ indicates the element-wise magnitude square of a vector, and γ is a unitless parameter introduced to tune the amount of regularization. The operator $\mathrm{var}(x)$, for any vector, x, is the sample variance defined as

$$\mathrm{var}(x) = \frac{1}{M}\sum_{i=1}^M \left(x_i - \frac{1}{M}\sum_{j=1}^M x_j\right)^2. \tag{51}$$

After the outer loop runs N_L times, we again reinitialize according to Eq. (50) and run the EM algorithm until it reaches the stopping threshold ϵ_T. We found that a Gaussian prior model worked best in the outer loop for the initialization of ϕ, especially at low SNRs. Specifically, we used $q = 2$, $p = 2$, $T = 1$, and $b = G(0.8)$, where $G(\sigma)$ indicates a 3×3 Gaussian kernel with standard deviation σ. Once the initialization process was complete, different prior-model parameters could be used for the actual reconstruction.

We conjecture that the proposed iterative process may help avoid local minima; however, this cannot be easily verified since evaluation of the cost function given in Eq. (7) would require the determinant and inversion of a $200^2 \times 200^2$ covariance matrix given by Eq. (6). As a result, evaluating the cost function to verify this idea is a non-tractable problem.

D. Complexity

The complexity of the proposed algorithm described in Fig. 6 is driven by the iterative updates of the five main

MBIR Algorithm $\{$

Inputs: $y,\ \gamma,\ q,\ p,\ T,\ b,\ N_K,\ N_L,\ \epsilon_T$

Outputs: $\hat{r}$

$\phi \leftarrow \hat{\phi}_{PGA}$

for $i = 1 : N_L$ **do**

   $r \leftarrow |A^H y|^{\circ 2},\ \sigma_r \leftarrow \frac{1}{\gamma}\sqrt{\mathrm{var}(r)},\ \sigma_w^2 \leftarrow \mathrm{var}(y)$

   $\phi \leftarrow$ **Iterative EM** $\left\{y, r, \phi, \sigma_r, \sigma_w^2, 2, 2, 1, G(0.8), N_K\right\}$

end for

$r \leftarrow |A^H y|^{\circ 2},\ \sigma_r \leftarrow \frac{1}{\gamma}\sqrt{\mathrm{var}(r)},\ \sigma_w^2 \leftarrow \mathrm{var}(y)$

$r \leftarrow$ **Iterative EM** $\left\{y, r, \phi, \sigma_r, \sigma_w^2, q, p, T, b, \epsilon_T\right\}$

$\}$

Fig. 7. Algorithm which initializes and runs the EM algorithm. An iterative process is used to initialize the phase error vector ϕ. $G(\sigma)$ indicates a 3×3 Gaussian kernel with standard deviation σ.
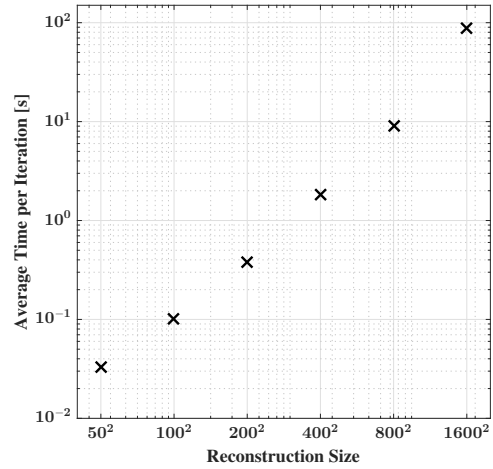

Fig. 8. Scalability of the proposed algorithm is shown to be linear in time with respect to the input/output size for $M = N$. The average time was computed from 10 iterations.

variables, μ, C, r, σ_w^2, and ϕ. In particular, updating μ, σ_w^2, and ϕ require multiplication by the forward-model operator, A_ϕ, which has a complexity $\mathcal{O}(N^2)$. Fortunately, the use of the NUFFT allows us to reduce the complexity to $\mathcal{O}(K \log N)$, where K is the length of the oversampled FFT used, and was set to $K = 2N$ in this work. Since we are limiting ourselves to cases where $A^H A = MI$, updating C becomes trivial using Eq. (41), which has a complexity $\mathcal{O}(N)$. The ICD updates of r also scale with complexity $\mathcal{O}(N)$.

Therefore, for very large N, the complexity of the proposed algorithm is dominated by the NUFFT and is on the order of $\mathcal{O}(K \log N)$. However, for practical values of N, the NUFFT is efficient, and the computation time is dominated by the ICD updates. Figure 8 shows the average time required for each iteration of the EM algorithm as a function of the input/output size for $M = N$. The reconstructions were run in MATLAB using a computer with a 2.6 GHz Intel Core i7 processor. The results show an approximately-linear increase in the computation time as a function of the input/output size.

V. RESULTS

In this section, results are presented for data generated from the AFRL simulation tool *SimISAL* [28], and from data produced in the ISAL laboratory at JPL [40], [41].

A. Simulated Data

SimISAL is a high-fidelity wave-optics MATLAB simulation tool used to simulate ISAL imaging of objects in space [28]. It models many of the physical effects that degrade real data as well as their dependent interactions, and was used to generate simulated data for the following experiments.

Fig. 9 shows a generic test pattern with an arbitrary grid size, L, that was chosen as the target. Subplot (a) shows the reflectance as a function of range, z, and cross-range, x, and Subplot (d) shows the corresponding velocity map. Table I specifies the parameters used for simulation and MBIR reconstruction. Phase errors were included by adding i.i.d. uniformly distributed phase to each pulse (i.e. all samples of a single pulse had the same phase error). Simulations were conducted for three different levels of measurement noise, which we denote as Case 1, Case 2, and Case 3. These cases correspond to medium, low, and very low SNR levels, where SNR is defined as

$$\text{SNR} = \frac{\text{var}(Ag)}{\text{var}(w)}, \tag{52}$$

and g is a single realization of the random reflection-coefficient vector, given the reflectance, r. This definition of SNR is approximately equal to the range-compressed carrier-to-noise ratio (CNR), which is typically used in assessing the performance of SAR/SAL autofocus algorithms [42], [43].

FBR images were formed according to

$$\hat{r}_{\text{FBR}} = |W_{\text{FFT}}\mathcal{D}(T)\mathcal{D}(\hat{\phi}_{PGA})y|^{\circ 2}, \tag{53}$$

where W_{FFT} is a two-dimensional FFT matrix, and T is $M \times 1$ vector of weights corresponding to a Taylor window produced in MATLAB. FESAR images were formed according to Sec. IV-C of [12] using the parameters given in Table V-A and the stopping criteria given by Eq. (48). Since the algorithm in [12] does not correct phase errors[2], we only compare FESAR results for cases when the phase errors were known.

To compute α, the unknown scaling constant between r and the reconstructions $\hat{r}$, we find the least squares fit given by

$$\alpha^* = \underset{\alpha}{\text{argmin}}\left\{||\alpha\hat{r} - r||^2\right\}. \tag{54}$$

We then measure the reconstruction distortion using normalized root mean square error (NRMSE) which we define as

$$\text{NRMSE} = \sqrt{\frac{||\alpha^*\hat{r} - r||^2}{||r||^2}}. \tag{55}$$

To emphasize a balance between the amount of regularization and the resolution, we also measured the Structural Similarity Index (SSIM) over an area with high-spatial frequency content.

---

[2]Phase error correction was incorporated into the point-based algorithms of [15], [16], [44], [45], but not for the feature-based algorithms of [12], [46], [47].
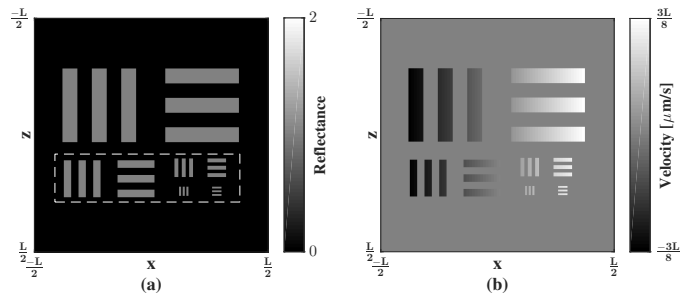

Fig. 9. Generic test pattern used for simulation input; (a) top-down view of the object's reflectance as a function of range, z, and cross-range, x, (b) the corresponding velocity map. The support of the test pattern is approximately square with width $3/4$ L, where L is the grid length. The input target array was sampled with period $L/1024$ in both dimensions. The white dotted line in (a) indicates the area containing high-spatial-frequency content that was used to optimize model parameters.

TABLE I
PARAMETERS OF SIMULATION AND RECONSTRUCTION FOR CASES 1-3

Item	Value	Units
Object Sampling Periods, δ_x, δ_z	$L/1024$	m
Rotation rate, $\dot{\theta}$	1	$\mu rad/s$
Wavelength, λ	1	μm
Chirp Rate, β	$200\pi c$	rad/s^2
Chirp length, τ_c	$1/(2L)$	s
PRF	$2L$	Hz
Acquisition Time, τ_s	$100/L$	s
Sample Period, τ_d	$1/(800L)$	s
Phase Error vector, ϕ	$\sim$ uniform$(-\pi, \pi)$	rad
Data Size, M	200^2	-
SNR *[Case 1, Case 2, Case 3]*	$[3, 1, 0.3]$	-
Reconstruction Size, N	200^2	-
Reconstruction Field of View	$L \times L$	m
Reconstruction Resolution, (ρ_x, ρ_z)	$(L/200, L/200)$	m
Reconstruction Filter, H	I	-
Neighborhood, b	3×3, $G(0.1)$	pixels
Regularization Tuning Parameter, γ	2	-
QGGMRF Parameter, q	2	-
QGGMRF Parameter, T	$[0.05, 0.05, 0.1]$	-
QGGMRF Parameter, p	1.1	-
Reinitialization Parameter, (N_L, N_k)	$(300, 10)$	iter
FESAR Scale Parameter, λ_1	$[0.5, 1.5, 2.0]$	-
FESAR Scale Parameter, λ_2	$[5.0, 3.0, 3.7]$	-
FESAR Parameter, ϵ	5×10^2	-
Stoping criteria, ϵ_T	1×10^{-4}	-

Specifically, we made measurements over the white-dotted region in Fig. 9 (a) using MATLAB's default SSIM function. For both FESAR and MBIR, the reconstruction parameters were chosen to maximize SSIM over this region. This ensured we obtained the highest quality reconstructions without blurring the smaller bars in the image.

1) Experiment 1: Variation of QGGMRF Parameters: To further illustrate how the QGGMRF parameters effect image quality, we used the simulated data from Case 1 and varied the reconstruction parameters from the nominal values shown in Table I. Figure 10 shows the results. The top row shows how the shape of the potential function changes the output. The top left is a quasi-TV reconstruction with $p = 1.1$ and $T = 0.05$, the top right is a Gaussian reconstruction with $p = 2$, and the middle is a hybrid of the two. The results show that the first reconstruction has sharper edges and reduced speckle variation. However, looking closely at the smaller bars, we

TABLE II

NRMSE AND SSIM FOR SIMULATIONS RESULTS (SR) 1 & 2

	Case #	NRMSE*			SSIM*		
		1	2	3	1	2	3
SR 1	FBR	1	1	1	1	1	1
	FERN	0.48	0.48	0.38	1.6	2.0	2.8
	MBIR	**0.42**	**0.34**	**0.33**	**4.4**	**4.7**	**4.0**
SR 2	FBR	1	1	1	1	1	1
	MBIR	**0.42**	**0.32**	**0.24**	**5.7**	**6.1**	**12.0**

* metics normalized by FBR value for comparison

see that they are starting to blur together, limiting the amount of regularization that can be applied, as shown in the bottom row. The Gaussian reconstruction in Fig 10 (c) preserves the smaller bars, but also allows residual speckle variation in the homogeneous areas.

The second row of Fig. 10 shows how the choice of scale parameter impacts the reconstruction. On the bottom left, we see that choosing a γ which is too small, under regularizes the image, leaving residual speckle variation. Conversely, on the bottom right we see that a large γ can reduce speckle variation, but can also blur image detail around the smaller bars.

2) Experiment 2: Comparison with Known Phase Errors: In the second experiment, we compare FBR, FESAR, and MBIR when phase errors are known a priori. Fig. 11 shows the resulting reconstructions for the parameters specified in Table I. The measured distortion metics are listed in the top part of Table II, normalized by the FBR value for easy comparison. FESAR significantly reduces the NRMSE compared to FBR. However, the smaller bars have been blurred and there still remains significant variation in the homogeneous areas. Conversely, the proposed MBIR technique produced lower NRMSE values than FESAR, but with less residual variation and blurring. This is highlighted by the higher SSIM values for MBIR. In all three cases, MBIR does an excellent job at increasing the contrast between the object and the background, and at reducing speckle variations without the need for incoherent averaging.

Ideally, we would like to gain insight into the convergence behavior of the proposed algorithm by plotting cost as a function of iteration number. Unfortunately our non-tractable cost function prohibits this. Instead we consider reconstruction error as a function of iteration number. Figure 12 (a) shows the NRMSE as a function of iteration number corresponding to the reconstructions in Fig. 11. We see that FESAR converges much quicker; however, the final NRMSE values are higher than those of MBIR. At the two higher SNRs, MBIR achieves a NRMSE equal to FESAR's final value in approximately the same number of iterations. For the lowest SNR, it takes MBIR approximately twice as many iterations to reach FESAR's final value. Figure 12 (a) also shows that we may be able to increase ϵ_T to reduce the number of MBIR iterations with little impact to the NRMSE.

3) Experiment 3: Comparison with Unknown Phase Errors: Using the same data, FBR and MBIR were run again with no prior knowledge of the phase error. Fig. 13 shows the results. The measured distortion metics are listed in the bottom

part of Table II. For these relatively low SNR values, PGA has difficulty correcting the i.i.d. uniform phase errors [43]. In Case 1, PGA is not able to estimate the higher-order components of the phase error, resulting in a blurred image. For the other two cases, it fails more drastically. The MBIR algorithm was able to produce focused images in all three cases. MBIR's NRMSE was 58-76% lower than that of FBR with PGA. In addition, when comparing Figs. 11 and 13, the results show that MBIR performed almost as well with no knowledge of the phase errors as it did when the errors were known.

Figure 12 (b) shows how the NRMSE changes when phase errors are not known and the reinitialization process is used. The spikes at iteration 3000 occur when switching from the final reinitialization loop to the actual reconstruction. They are a result of switching from the Gaussian prior used to initialize the phase errors, to a prior which more-closely resembles an L1 norm during reconstruction. Figure 12 (b) also reveals that the number of reinitialization loops N_L can be reduced without significantly impacting NRMSE. However, caution must be exercised since NRMSE does not necessarily correspond to changes in the cost function nor does it indicate a focused image.

B. Laboratory Data

In this section, the proposed MBIR technique was tested on data produced in the ISAL laboratory at JPL [40], [41]. The bench-top experimental setup was a bi-static system consisting of a transmitter, heterodyne receiver, and rotating target. A 1310 nm tunable laser produced a LFM chirped pulse using a PZT actuator to tune the laser's external cavity [41]. A self heterodyning system was employed where 10% of the transmitted signal was used as the local oscillator. Specific details about the system are provided in Table III. To isolate the narrow-band signal of interest, the detected signal is demodulated, low-pass filtered, and down sampled, resulting in M data points.

Various shaped target stencils were placed on a Spectralon plate angled at 45 degrees which acted as a Lambertian reflector in the near infrared (IR). A rotation stage actuated by a PZT was used to provide relative movement between the transmitter/receiver and target. The target platform is shown in Fig. 14. Three different target stencils were used in this experiment, a simple three-bar target, the Air Force logo, and the same test pattern used in the simulations. They are shown in the top row of Fig. 15.

There are four attributes of the experimental setup that degrade, alter, or limit the performance of the imaging system, and therefore make image reconstruction more difficult.

1) Although there were no phase errors purposely induced, the combination of a less-than-perfect waveform and an open air system (i.e the beam passes through several meters of free-flowing laboratory air) generate phase errors and blur the image.

2) At IR wavelengths the paper used for the stencils and to block the stage is both slightly reflective and translucent. This results in background clutter (similar
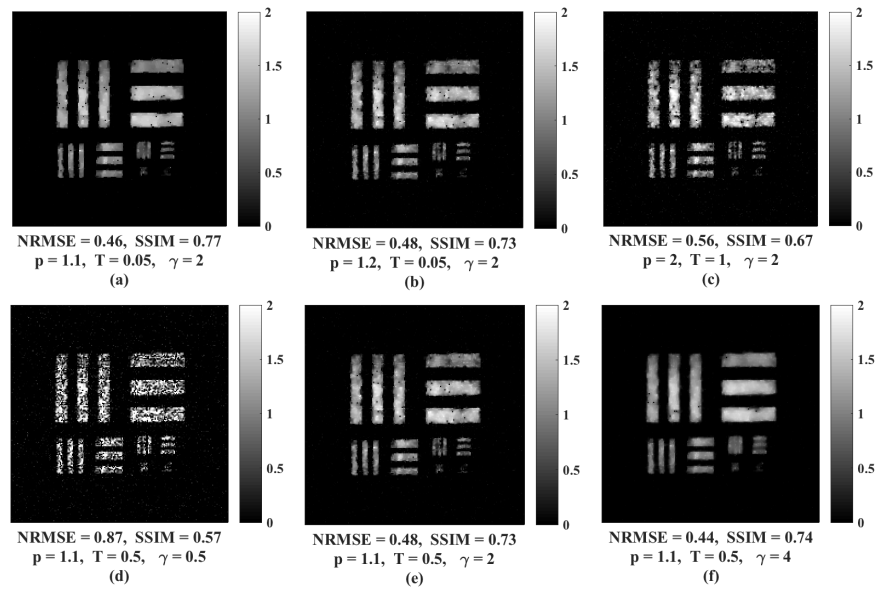
Fig. 10. Results for Experiment 1 showing the impact of QGGMRF parameters, (p, T, γ), on reconstruction. The top row shows the difference between (a) a quasi-TV reconstruction, (b) a hybrid reconstruction, and (c) a Gaussian reconstruction. The bottom row shows the effect of varying γ which controls the amount of regularization. The vertical axes represent range and the horizontal represent cross-range.
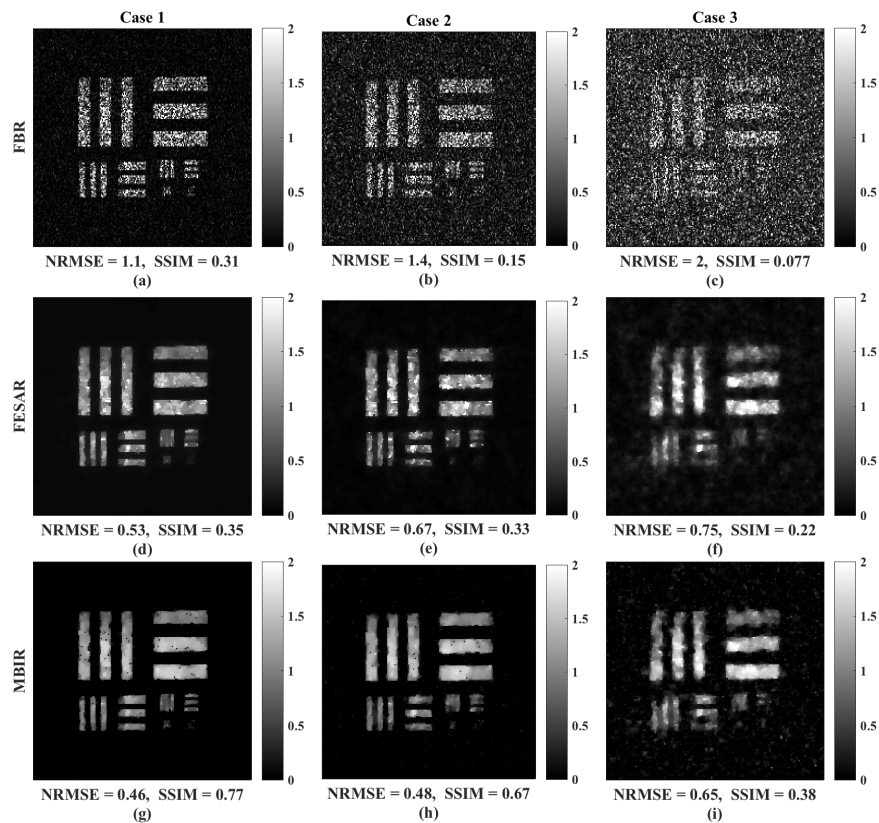

Fig. 11. Results for Experiment 2 comparing FBR (a-c), FESAR (d-f), and MBIR (g-i) for SNR levels of 3, 0.9, and 0.33 when phase errors were known a priori. The vertical axes represent range and the horizontal represent cross-range.

to what a ground-looking SAL system might encounter) and returns from objects behind the paper barrier.

3) The target plate was aligned by eye and the card-stock had a slight tilt across it (i.e. it may not be completely flush to the plate). Therefore the image appears skewed or rotated. The effect is similar to having an axis of rotation which is not parallel to the y-axis.

4) Lastly, the resolution was poor relative to the target size and detail.

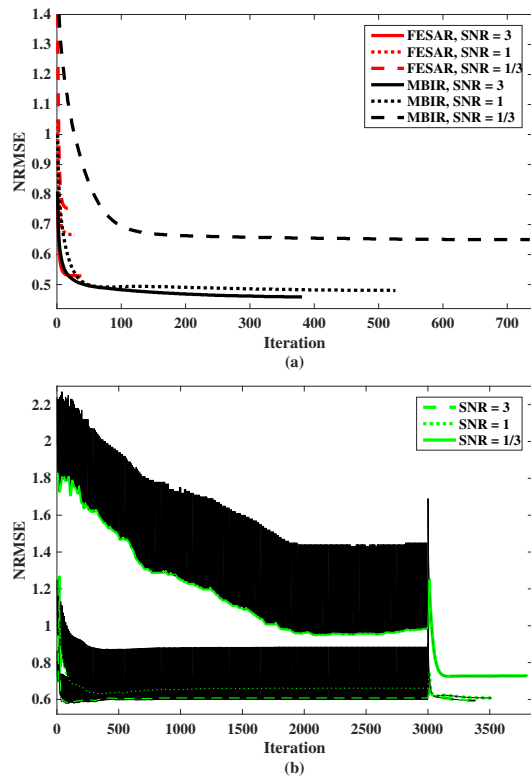While these issues make reconstruction more difficult, they

Fig. 12. Reconstruction error versus iteration number for (a) Experiment 2 and (b) Experiment 3. The green, bold lines in (b) plot every 10th sample to highlight the trend. The spikes at iteration $k = 3000$ result from using different parameters for the reinitialization process and the reconstruction.

TABLE III
PARAMETERS OF LABORATORY SETUP AND RECONSTRUCTION FOR THE THREE-BAR TARGET, LOGO, AND TEST PATTERN, RESPECTIVELY

Item	Value	Units
Wavelength, λ	1.31	μm
Rotation rate, $\dot{\theta}$	12.5	$\mu rad/s$
Chirp Rate, β/π	2	THz/s
Chirp length, τ_c	34	ms
PRF	10	Hz
Acquisition Time, τ_s	60	s
Sample Rate, τ_d^{-1}	1	MHz
Data Size, M	$[79^2, 41^2, 50^2]$	-
Reconstruction Size, N	$[79^2, 41^2, 50^2]$	-
Reconstruction Resolution, (ρ_x, ρ_z)	$(0.88, 2.3)$	mm
Reconstruction Filter, H	I	-
Neighborhood, b	3×3, $G(0.8)$	pixels
Regularization Tuning Parameter, γ	2	-
QGGMRF Parameter, q	2	-
QGGMRF Parameter, T	$[0.1,\ 0.5,\ 0.5]$	-
QGGMRF Parameter, p	1.1	-
Reinitialization Parameters, $(N_L,\ N_k)$	$(300,\ 10)$	iter
Stoping criteria, ϵ_T	1×10^{-4}	-

helped highlight the strength of the proposed MBIR technique compared to FBR in such limiting conditions.

Looking at the FBR reconstructions in Fig. 15, subplots (d) through (f), we see that the three-bar target is focused and is recognizable, but still has some minimal background clutter. The logo appears focused, but has significant background clutter, making it difficult to identify the target or determine its support. The test pattern is unrecognizable with significant

background clutter.

The MBIR reconstructions are shown in subplots (g) through (i). In all three cases, the support of the object is more clearly established, the object-background contrast is higher, and the speckle variation is reduced. In addition, the large three-bar targets in the test pattern are visible and recognizable in the MBIR reconstruction but not in the FBR image.

VI. CONCLUSION

In this paper we have presented a model-based iterative reconstruction algorithm designed specifically for SAL. Rather than estimating the speckled reflection coefficient, we proposed estimating the real-valued reflectance. This represents a more-direct approach for producing reconstructions which closely resemble conventional optical images. A Bayesian framework was used to derive the MAP estimate of the reflectance. Using a QGGMRF prior model, we were able to model two-dimensional correlations between neighboring pixels, which promoted a smooth and more natural looking reconstruction. The EM algorithm was used to design a surrogate function which simplified the optimization process.

The utility of the proposed algorithm was verified using simulated data from AFRL's *SimISAL*, as well as experimental data from JPL's ISAL Laboratory. Results showed significant and consistent improvements over conventional reconstructions in terms of image contrast, speckle reduction, autofocus, and low-noise performance. The challenging laboratory conditions highlight the ability of the proposed MBIR algorithm to form images which make object characterization and identification much easier than it is for FBR images. The ability to distinguish objects from the background, reduce speckle variations, and resolve basic features, even in strong noise or clutter, are key to this difference.

APPENDIX A
FURTHER ANALYSIS OF SIGNAL PHASE

In this section, we show that the phase term $4\beta t\tilde{\varphi}(t)x/c$ in Eq. (17) can be neglected when

$$\rho_z \gg \lambda N_x, \tag{56}$$

where ρ_z is the resolution of the system along the range (z) dimension, given by

$$\rho_z = \frac{\pi c}{2\beta\tau_c}, \tag{57}$$

λ is the illumination wavelength, and N_x is the number of samples in the cross-range (x) dimension. If we define x_{max} as the maximum extent of the object in the x dimension, the number of cross-range samples is given by

$$N_x = \frac{2\tilde{\varphi}(t)x_{max}}{\lambda}, \tag{58}$$

Given x_{max} and Eqs. (57) and (58), we can specify an upper limit on the phase term given by

$$\begin{aligned}
\frac{4\beta t\tilde{\varphi}(t)x}{c} &\leq \frac{4\beta t\tilde{\varphi}(t)x_{max}}{c}, \\
&= \left(\frac{2\lambda\beta\tau_c}{c}\right)\left(\frac{2\tilde{\varphi}(t)x_{max}}{\lambda}\right). \\
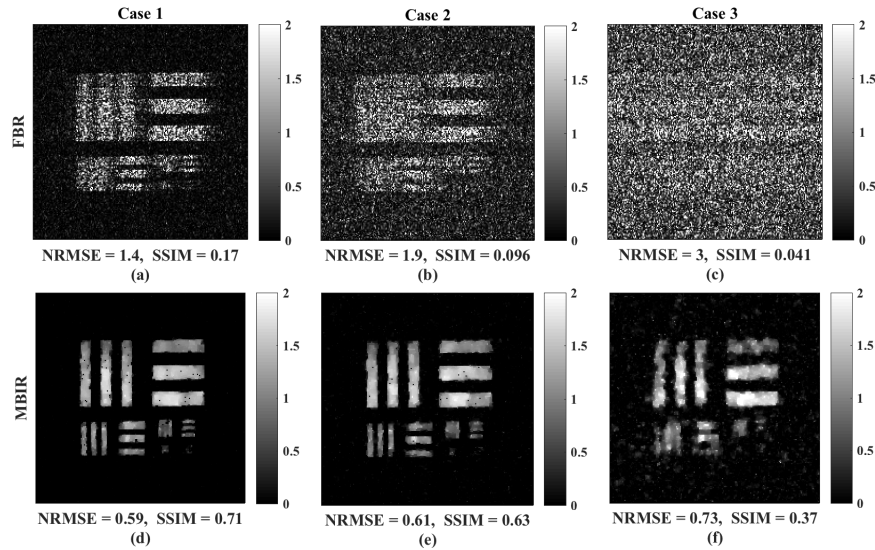&= \pi\lambda\frac{1}{\rho_z}N_x\ .
\end{aligned} \tag{59}$$

Fig. 13. Results for Experiment 3 comparing FBR (a-c) and MBIR (d-f) for SNR levels of 3, 1, and 0.3 when phase errors were not known a priori. The vertical axes represent range and the horizontal represent cross-range. FESAR was not included since it does not correct phase errors.
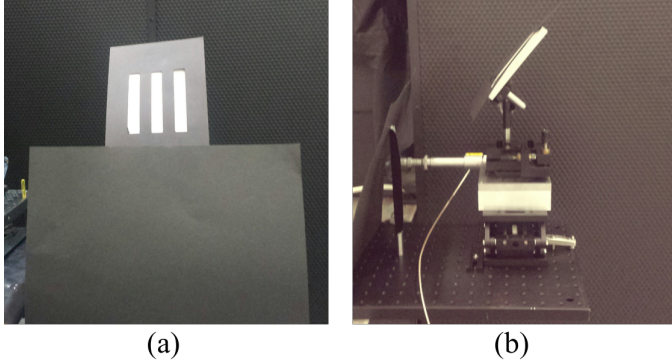

Fig. 14. Target platform used for laboratory setup when viewed from the front (a) and side (b). A stencil made of matt black cardstock paper on top of a white Spectralon reflecting plate was used as a target. Matt black paper was also used to block returns from the rotation stage.

To be considered negligible, the upper limit given in Eq. (59) must be small. Specifically, we will require that

$$\pi\lambda\frac{1}{\rho_z}N_x \ll \pi \qquad (60)$$

By rearranging Eq. (60), we get the constraint given by Eq. (56). For an example scenario where $N_x = 200$ and $\lambda = 1 \times 10^{-6}$, we get an easy-to-achieve constraint of

$$\rho_z \gg 2 \times 10^{-4} \ . \qquad (61)$$

APPENDIX B
EVALUATION OF GRAM MATRIX

In order to use Eq. (41), we must show that $A^H A = MI$. In this section, we first specify the structure of A, then show the (r, s) element of the Gram matrix is $(A^H A)_{r,s} = M\delta(r - s)$.

We start with our definition of the forward model operator, A, given in Eq. (32) and the following three assumptions about its structure: 1) We assume the signal is band limited and

Nyquist sampled. This allows us to express the reconstruction-filter as $H = I$. 2) We assume that A is a square matrix. For this to be true, we must reconstruct images which are the same size as the data (i.e. $M = N$). 3) We must assume some function for the object rotation angle $\varphi(p, q)$ in order to evaluate the structure of A. We choose a simple linear model given by

$$\varphi(p, q) = \dot{\varphi}t = \dot{\varphi}p\tau_c + \dot{\varphi}q\tau_d, \qquad (62)$$

where $\dot{\varphi}$ is the object-rotation rate in rad/s, and $t = p\tau_c + q\tau_d$ is the time of the qth sample of the pth pulse.

Given the definition of A in Eq. (32) and assumption 1 above, the Gram matrix can be written as

$$A^H A = D^H H^H \mathcal{D}(\phi)^H \mathcal{D}(\phi) H D = D^H D, \qquad (63)$$

where ϕ is the phase-error vector of unit-amplitude exponentials, and therefore $\mathcal{D}(\phi)^H \mathcal{D}(\phi) = I$. The matrix D represents the skewed DSFT of Eq. (28). To show that $A^H A = MI$, it is sufficient to show that $D^H D = MI$. We do so by deriving an explicit expression for D given assumptions 2 and 3, then evaluating the elements of its Gram matrix $D^H D$.

To derive an expression for D, we start with Eq. (28), which we will write as

$$\mathbf{G}(q, p) = \sum_{l=0}^{N_z-1} \sum_{k=0}^{N_x-1} \mathbf{g}(l, k)e^{j2\pi\left[\frac{2\varphi(p,q)\tau_c\delta_x}{\lambda}k + \frac{\beta\tau_d\delta_z q}{\pi c}l\right]}, \qquad (64)$$

where boldface type is used to represent the two-dimensional forms of vectors $G \in \mathbb{C}^M$ and $g \in \mathbb{C}^N$, and $G = Dg$. For N_q samples per pulse and N_p pulses, $\mathbf{G} \in \mathbb{C}^{N_q \times N_p}$. Additionally, for a reconstruction with N_z samples along the z dimension and N_x samples along the x dimension, $\mathbf{g} \in \mathbb{C}^{N_z \times N_x}$. Using assumption 2, we have $N_z = N_q$ and $N_x = N_p$, and the image-domain sample periods are equal to the FBR resolutions given by [8]

$$\delta_x = \frac{\lambda}{2\dot{\varphi}\tau_c N_x}, \qquad\qquad \delta_z = \frac{\pi c}{\beta\tau_d N_z} \ . \qquad (65)$$
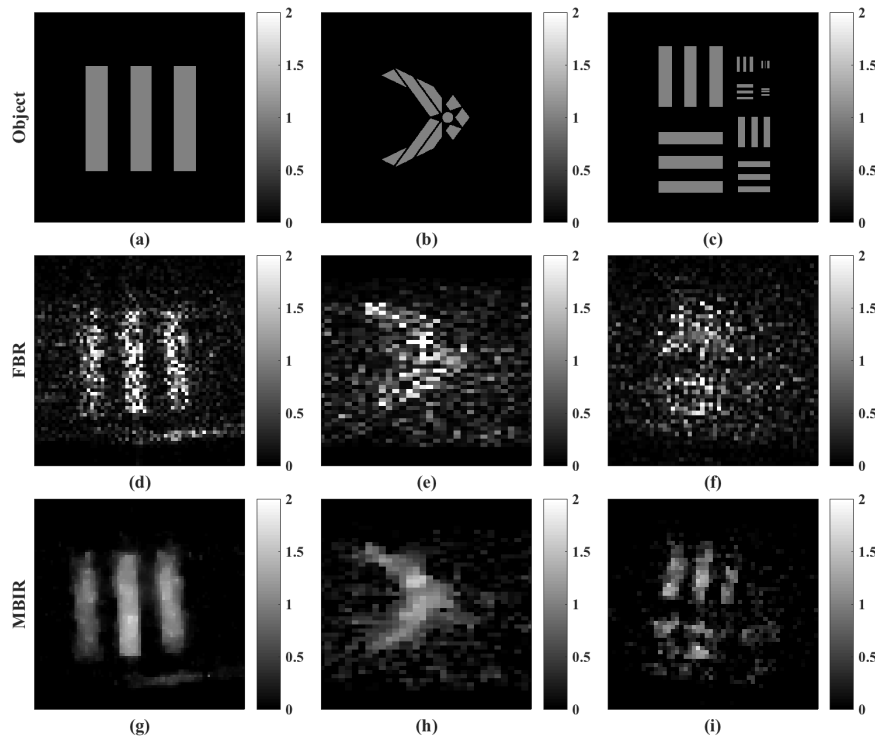
Fig. 15. Target stencils used in laboratory experiment (a-c), FBR reconstructions with PGA autofocus (d-f), and MBIR reconstructions (g-i). The vertical axes represent range and the horizontal represent cross-range. FESAR was not included since it does not correct phase errors.

Using Eqs. (62) and (65), and noting that the ratio of the detector sample period to the pulse length is given by $\tau_d/\tau_c = 1/N_z$, we can write Eq. (64) as

$$\mathbf{G}(q,p) = \sum_{l=0}^{N_z-1} \sum_{k=0}^{N_x-1} \mathbf{g}(l,k) e^{j\frac{2\pi}{N_x}kp} e^{j\frac{2\pi}{N_xN_z}kq} e^{j\frac{2\pi}{N_z}lq} . \quad (66)$$

Equation (66) gives the relationship between the two-dimensional functions $\mathbf{G}$, and $\mathbf{g}$. We now use Eq. (66) to determine the relationship between the vectors G and g, which is represented by the matrix D. For raster ordering, the element $D_{m,n}$ relates the vector element $g_n = \mathbf{g}(\lfloor n/N_x \rfloor, \mathrm{mod}\{n, N_x\})$ to $G_m = \mathbf{G}(\lfloor m/N_x \rfloor, \mathrm{mod}\{m, N_x\})$, where $\lfloor \cdot \rfloor$ indicates the floor operator, and $\mathrm{mod}\{\cdot\}$ indicates the modulo operator. Therefore, using the kernel from Eq. (66), we can write the (m,n) element of D as

$$D_{m,n} = e^{j\frac{2\pi}{N_x}\mathrm{mod}\{n,N_x\}\mathrm{mod}\{m,N_x\}} e^{j\frac{2\pi}{N_xN_z}\mathrm{mod}\{n,N_x\}\lfloor\frac{m}{N_x}\rfloor}$$
$$* e^{j\frac{2\pi}{N_z}\lfloor\frac{n}{N_x}\rfloor\lfloor\frac{m}{N_x}\rfloor} . \quad (67)$$

Given Eq. (67), we can express element r,s of the Gram matrix as

$$(D^HD)_{r,s} = \sum_{i=0}^{M-1} D^*_{i,r} D_{i,s},$$
$$= \sum_{i=0}^{M-1} e^{j\frac{2\pi}{N_x}c_1\mathrm{mod}\{i,N_x\}} e^{j\frac{2\pi}{N_z}c_2\lfloor\frac{i}{N_x}\rfloor}, \quad (68)$$

where

$$c_1 = \mathrm{mod}\{s, N_x\} - \mathrm{mod}\{r, N_x\}, \quad (69)$$

and

$$c_2 = \lfloor\frac{s}{N_x}\rfloor - \lfloor\frac{r}{N_x}\rfloor + \frac{\mathrm{mod}\{s, N_x\} - \mathrm{mod}\{r, N_x\}}{N_x}, \quad (70)$$

are are constant with respect to the index variable i.

Next, we split the sum over i into a two dimensional sum over $i_z = \lfloor i/N_x \rfloor$ and $i_x = \mathrm{mod}\{i, N_x\}$. This allows us to represent Eq. (68) as the product of two geometric sums given by

$$(D^HD)_{r,s} = \sum_{i_z=0}^{N_z-1} \left(e^{j\frac{2\pi}{N_z}c_2}\right)^{i_z} \sum_{i_x=0}^{N_x-1} \left(e^{j\frac{2\pi}{N_x}c_1}\right)^{i_x} . \quad (71)$$

For the diagonal elements of the gram matrix, $r = s$, which results in $c_1 = c_2 = 0$, and $(D^HD)_{s,s} = N_z * N_x = M$. For cases where $r \neq s$, we can use a geometric sum to write Eq. (71) as

$$(D^HD)_{r\neq s} = \frac{1 - \left(e^{j\frac{2\pi}{N_z}c_2}\right)^{N_z}}{1 - e^{j\frac{2\pi}{N_z}c_2}} * \frac{1 - \left(e^{j\frac{2\pi}{N_x}c_1}\right)^{N_x}}{1 - e^{j\frac{2\pi}{N_x}c_1}}$$
$$= \frac{1 - \left(e^{j2\pi}\right)^{c_2}}{1 - e^{j\frac{2\pi}{N_z}c_2}} * \frac{1 - \left(e^{j2\pi}\right)^{c_1}}{1 - e^{j\frac{2\pi}{N_x}c_1}}, \quad (72)$$
$$= 0 .$$

Therefore, $(D^HD)_{r,s} = M\delta(r-s)$, and $A^HA = MI$.

Laboratory. Views expressed in this paper are those of the authors and do not reflect the official policy of the Air Force, the Department of Defense, or the U.S. Government

REFERENCES

[1] R. L. Lucke and L. J. Rickard, "Photon-limited synthetic aperture imaging for planet surface studies," *Applied Optics*, vol. 41, no. 24, pp. 5,084–5,095, 2002.

[2] S. M. Beck, J. R. Buck, W. F. Buell, R. P. Dickinson, D. A. Kozlowski, N. J. Marechal, and T. J. Wright, "Synthetic-aperture imaging laser radar: laboratory demonstration and signal processing," *Applied optics*, vol. 44, no. 35, pp. 7621–7629, 2005.

[3] W. Buell, N. Marechal, J. Buck, R. Dickinson, D. Kozlowski, T. Wright, and S. Beck, "Demonstration of synthetic aperture imaging ladar," in *Defense and Security*. International Society for Optics and Photonics, 2005, pp. 152–166.

[4] B. Krause, J. Buck, C. Ryan, D. Hwang, P. Kondratko, A. Malm, A. Gleason, and S. Ashby, "Synthetic aperture ladar flight demonstration," in *CLEO: Science and Innovations*. Optical Society of America, 2011, p. PDPB7.

[5] S. Crouch and Z. W. Barber, "Laboratory demonstrations of interferometric and spotlight synthetic aperture ladar techniques," *Optics express*, vol. 20, no. 22, pp. 24 237–24 246, 2012.

[6] Z. W. Barber and J. R. Dahl, "Synthetic aperture ladar imaging demonstrations and information at very low return levels," *Applied optics*, vol. 53, no. 24, pp. 5531–5537, 2014.

[7] M. A. Richards, *Fundamentals of radar signal processing*. Tata McGraw-Hill Education, 2005.

[8] C. V. Jakowatz, *Spotlight-Mode Synthetic Aperture Radar, A Signal Processing Approach*. New York New York: Springer Science+Business Media, Inc., 1996.

[9] J. W. Goodman, *Statistical Optics*. New York New York: John Wiley and Sons Inc, 1985.

[10] E. Hecht, *Optics*, ser. Pearson education. Addison-Wesley, 2002. [Online]. Available: https://books.google.com/books?id=T3ofAQAAMAAJ

[11] J. W. Goodman, *Speckle Phenomena in Optics, Theory and Applications*. Englewood Colorado: Roberts and Company, 2006.

[12] M. Cetin and W. C. Karl, "Feature-enhanced synthetic aperture radar image formation based on nonquadratic regularization," *Image Processing, IEEE Transactions on*, vol. 10, no. 4, pp. 623–631, 2001.

[13] L. C. Potter, P. Schniter, and J. Ziniel, "Sparse reconstruction for radar," in *SPIE Defense and Security Symposium*. International Society for Optics and Photonics, 2008, pp. 697 003–697 003.

[14] L. C. Potter, E. Ertin, J. T. Parker, and M. Cetin, "Sparsity and compressed sensing in radar imaging," *Proceedings of the IEEE*, vol. 98, no. 6, pp. 1006–1020, 2010.

[15] N. Ö. Önhon and M. Cetin, "Joint sparsity-driven inversion and model error correction for radar imaging," in *Acoustics Speech and Signal Processing (ICASSP), 2010 IEEE International Conference on*. IEEE, 2010, pp. 1206–1209.

[16] M. Cetin, I. Stojanovic, N. O. Onhon, K. R. Varshney, S. Samadi, W. C. Karl, and A. S. Willsky, "Sparsity-driven synthetic aperture radar imaging: Reconstruction, autofocusing, moving targets, and compressed sensing," *Signal Processing Magazine, IEEE*, vol. 31, no. 4, pp. 27–40, 2014.

[17] S. Ugur and O. Arikan, "Sar image reconstruction and autofocus by compressed sensing," *Digital Signal Processing*, vol. 22, no. 6, pp. 923–932, 2012.

[18] G. Xu, M. Xing, L. Zhang, Y. Liu, and Y. Li, "Bayesian inverse synthetic aperture radar imaging," *Geoscience and Remote Sensing Letters, IEEE*, vol. 8, no. 6, pp. 1150–1154, 2011.

[19] D. Vu, M. Xue, X. Tan, and J. Li, "A bayesian approach to sar imaging," *Digital Signal Processing*, vol. 23, no. 3, pp. 852–858, 2013.

[20] L. Zhao, L. Wang, G. Bi, and L. Yang, "An autofocus technique for high-resolution inverse synthetic aperture radar imagery," *Geoscience and Remote Sensing, IEEE Transactions on*, vol. 52, no. 10, pp. 6392–6403, 2014.

[21] W. Su, H. Wang, B. Deng, Y. Qin, and Y. Ling, "High resolution of isar imaging based on enhanced sparse bayesian learning," in *Signal Processing (ICSP), 2014 12th International Conference on*. IEEE, 2014, pp. 2063–2067.

[22] W.-g. Su, H.-q. Wang, B. Deng, R.-j. Wang, and Y.-l. Qin, "Sparse bayesian learning in isar tomography imaging," *Journal of Central South University*, vol. 22, pp. 1790–1800, 2015.

[23] X. Ren and X. Sun, "An algorithm for inverse synthetic aperture imaging lidar based on sparse signal representation," *Laser Physics*, vol. 24, no. 12, p. 125007, 2014.

[24] M. E. Tipping, "Sparse bayesian learning and the relevance vector machine," *The journal of machine learning research*, vol. 1, pp. 211–244, 2001.

[25] D. G. Tzikas, A. C. Likas, and N. P. Galatsanos, "The variational approximation for bayesian inference," *Signal Processing Magazine, IEEE*, vol. 25, no. 6, pp. 131–146, 2008.

[26] C. Pellizzari and C. A. Bouman, "Inverse synthetic aperture ladar image construction: An inverse model-based approach." SPIE Optics + Photonics, 2016.

[27] J. B. Thibault, K. Sauer, C. Bouman, and J. Hsieh, "A three-dimensional statistical approach to improved image quality for multi-slice helical ct." *Medical Physics*, vol. 34, no. 11, pp. 4526–4544, November 2007.

[28] C. Pellizzari, M. Spencer, N. Steinhoff, J. Belsher, G. Tyler, S. Williams, and S. Williams, "Inverse synthetic aperture ladar: a high-fidelity modeling and simulation tool," in *SPIE Optical Engineering+ Applications*. International Society for Optics and Photonics, 2013, pp. 88 770B–88 770B.

[29] S. M. Kay, *Fundamentals of Statistical Signal Processing, Detection Theory*. Prentice Hall Signal Processing Series, 1993, vol. II.

[30] A. P. Dempster, N. M. Laird, and D. B. Rubin, "Maximum likelihood from incomplete data via the em algorithm," *Journal of the royal statistical society. Series B (methodological)*, pp. 1–38, 1977.

[31] C. J. Wu, "On the convergence properties of the em algorithm," *The Annals of statistics*, pp. 95–103, 1983.

[32] R. A. Redner and H. F. Walker, "Mixture densities, maximum likelihood and the EM algorithm," *SIAM review*, vol. 26, no. 2, pp. 195–239, 1984.

[33] C. A. Bouman, *Model Based Image Processing*. Unpublished, 2015.

[34] A. N. Tikhonov and V. Y. Arsenin, "Solutions of ill-posed problems," 1977.

[35] D. Fink, "Coherent detection signal-to-noise," *Applied Optics*, vol. 14, no. 3, pp. 689–690, 1975.

[36] J. A. Fessler and B. P. Sutton, "Nonuniform fast fourier transforms using min-max interpolation," *Signal Processing, IEEE Transactions on*, vol. 51, no. 2, pp. 560–574, Feb 2003.

[37] P. J. Green, "Bayesian reconstructions from emission tomography data using a modified em algorithm," *IEEE transactions on medical imaging*, vol. 9, no. 1, pp. 84–93, 1990.

[38] R. Stevenson and E. Delp, "Fitting curves with discontinuities," in *Proc. of the first international workshop on robust computer vision*, 1990, pp. 127–136.

[39] J. Besag, "Towards bayesian image analysis," *Journal of Applied statistics*, vol. 20, no. 5-6, pp. 107–119, 1993.

[40] R. Trahan, B. Nemati, H. Zhou, M. Shao, I. Hahn, and W. Schulze, "Low cnr inverse synthetic aperture ladar imaging demonstration with atmospheric turbulence," in *Defense + Commercial Sensing, 2016 SPIE*. SPIE, 2016.

[41] R. Trahan, H. Zhou, B. Nemati, M. Shao, and W. Schulze, "Low cost chirp linearization for long-range isal imaging application," in *Defense + Commercial Sensing, 2016 SPIE*. SPIE, 2016.

[42] T. J. Karr, "Synthetic aperture ladar for planetary sensing," in *Optical Science and Technology, SPIE's 48th Annual Meeting*. International Society for Optics and Photonics, 2003, pp. 44–52.

[43] C. J. Pellizzari, J. Bos, M. F. Spencer, S. Williams, S. E. Williams, B. Calef, and D. C. Senft, "Performance characterization of phase gradient autofocus for inverse synthetic aperture ladar," in *Aerospace Conference, 2014 IEEE*. IEEE, 2014, pp. 1–11.

[44] N. Ö. Önhon and M. Cetin, "A nonquadratic regularization-based technique for joint sar imaging and model error correction," in *SPIE Defense, Security, and Sensing*. International Society for Optics and Photonics, 2009, pp. 73 370C–73 370C.

[45] N. Ö. Onhon and M. Cetin, "A sparsity-driven approach for joint sar imaging and phase error correction," *IEEE Transactions on Image Processing*, vol. 21, no. 4, pp. 2075–2088, 2012.

[46] M. Cetin, W. C. Karl, and A. S. Willsky, "Edge-preserving image reconstruction for coherent imaging applications," in *Image Processing. 2002. Proceedings. 2002 International Conference on*, vol. 2. IEEE, 2002, pp. II–481.

[47] ——, "Feature-preserving regularization method for complex-valued inverse problems with application to coherent imaging," *Optical Engineering*, vol. 45, no. 1, pp. 017 003–017 003, 2006.

Casey J. Pellizzari received a BSEE from California State University, Fullerton in 2005 and a MSEE in Electro-Optics at the Air Force Institute of Technology (AFIT) in 2010. His professional experience includes serving as a systems engineer and project manager at the Air Force Electronic Systems Center (ESC), Bedford, MA and as Deep Space Imaging Lead for the Directed Energy Directorate, Air Force Research Laboratory (AFRL), Kihei, HI. Major Pellizzari is currently a PhD candidate in the Electrical and Computer Engineering (ECE) department at Purdue University as part of the AFIT Civilian Institute (CI) program. His research interest include optically-coherent imaging systems, beam propagation through turbulent mediums, non-traditional imaging techniques, and signal processing.

Russell Trahan, III received his PhD in aerospace engineering from Texas A&M University in 2014 under the supervision of Dr. David Hyland. He also received a BS and MS in 2010 and 2012 at Texas A&M. His graduate research included space-borne optical interferometry, optimal control methods, system estimation, and computational methods for large degree-of-freedom real-time simulations. He currently works at the NASA Jet Propulsion Laboratory in the optics division's Advanced Optical Instruments section.

Hanying Zhou received her Ph.D. in Electrical Engineering from The Pennsylvania State University, and has been with Jet Propulsion Laboratory since 1998. Her current interests include telescope and coronagraph optics modeling and wavefront sensing and control, near-earth objects detection with a synthetic tracking camera, near-earth objects imaging with inverse synthetic aperture lidar. Previously, she has extensive research experience in holographic data storage, optical correlator and pattern recognition, and image and data analysis in general.

Skip Williams received joint BS degrees in Chemistry and Physics from the University of Arkansas in 1988 and a Ph.D. in Chemical Physics from Stanford University in 1994. Part of his Ph.D. thesis work was completed at the Combustion Research Facility at Sandia National Laboratories, and he started his research career with a Postdoctoral appointment at Los Alamos National Laboratory from 1994-1996. Since 1996, he has conducted research at the Air Force Research Laboratory and is currently the Chief Engineer at the Air Force Maui Optical and Supercomputing (AMOS) site. His current research focusses on inverse synthetic aperture LADAR for imaging space assets beyond the normal resolvable range of optics based on aperture diameter encompassing electro-optics, laser propagation, adaptive optics, and signal processing activities. He has published over 50 journal papers and is an Associate Fellow of the American Institute of Aeronautics and Astronautics (AIAA).

Stacie E. Williams of the Air Force Office of Scientific Research (AFOSR) manages the USAF's basic research investment in remote sensing with applications to space situational awareness and combat identification. This includes electro-optical imaging, astrodynamics, tracking, and atmospheric effects on beam control. Before coming to AFOSR she was the Technical Advisor to the Air Force Maui and Optical Supercomputing site where she managed the research and development programs. She has over 30 peer reviewed journal publications and received her Ph.D. from the University of California at Santa Cruz.

Bijan Nemati received his PhD in high energy physics from the University of Washington in 1990. Since 2001 he has helped develop advanced technologies for electromagnetic and optical sensing at NASA's Jet Propulsion Laboratory. He is currently the integrated modeling lead for the Wide-Field Infrared Survey Telescope.

Michael Shao has spent most of his career working on long baseline optical interfereomters, from several interferometers on Mt Wilson, and Palomar to the Keck Interferometer linking the two 10m telescopes on Mauna Kea, as well as technologies for space interferometry. More recently he has branched into two other areas, synthetic aperture LIDAR, and synthetic tracking, a technique to detect faint moving objects by coadding video frames with a shift/add approach along 1000's of velocity vectors.

Charles A. Bouman received a B.S.E.E. degree from the University of Pennsylvania in 1981 and a MS degree from the University of California at Berkeley in 1982. From 1982 to 1985, he was a full staff member at MIT Lincoln Laboratory and in 1989 he received a Ph.D. in electrical engineering from Princeton University. He joined the faculty of Purdue University in 1989 where he is currently the Showalter Professor of Electrical and Computer Engineering and Biomedical Engineering. He also is a founding co-director of Purdue's Magnetic Resonance Imaging Facility located in Purdue's Research Park. Professor Bouman's research is in statistical signal and image processing in applications ranging from medical to scientific and consumer imaging. His research resulted in the first commercial model-based iterative reconstruction (MBIR) system for medical X-ray computed tomography (CT), and he is co-inventor on over 47 issued patents that have been licensed and used in millions of consumer imaging products. Professor Bouman is a member of the National Academy of Inventors, a Fellow of the IEEE, a Fellow of the American Institute for Medical and Biological Engineering (AIMBE), a Fellow of the society for Imaging Science and Technology (IS&T), a Fellow of the SPIE professional society. He is the recipient of the 2014 Electronic Imaging Scientist of the Year award, and the IS&T's Raymond C. Bowman Award. He has been a Purdue University Faculty Scholar and received the College of Engineering Engagement/Service Award, and Team Award. He was previously the Editor-in-Chief for the IEEE Transactions on Image Processing, a Distinguished Lecturer for the IEEE Signal Processing Society, and the Vice President of Technical Activities for IEEE Signal Processing Society. He has been an associate editor for the IEEE Transactions on Image Processing and the IEEE Transactions on Pattern Analysis and Machine Intelligence. He has also been a Vice President of Publications and a member of the Board of Directors for the IS&T Society, and he is the founder and Co-Chair of the SPIE/IS&T conference on Computational Imaging.